ISSN 1027-4510, Journal of Surface Investigation: X-ray, Synchrotron and Neutron Techniques, 2024, Vol. 18, No. 3, pp. 633–640. © Pleiades Publishing, Ltd., 2024.

Using of Machine Learning Capabilities to Predict Double Phosphate Structures for Biomedical Applications

E. R. Kolomenskaya[a, *], V. V. Butova[a, b], Yu. V. Rusalev[a], B. O. Protsenko[a], A. V. Soldatov[a], and M. A. Butakova[a]

[a] *International Research Institute of Smart Materials, Southern Federal University, Rostov-on-Don, 344090 Russia*
[b] *Institute of General and Inorganic Chemistry, Bulgarian Academy of Sciences, Sofia, 1113 Bulgaria*
**e-mail: kolomenskaya@sfedu.ru*

Received December 12, 2023; revised February 2, 2024; accepted February 2, 2024

Abstract—In the rapidly developing field of biomedical research, the search for new materials with improved properties is crucial to moving the entire field forward. Double phosphates have generated significant interest in a wide range of applications, ranging from drug delivery systems to catalysts for biomedical reactions, and the fields of biomedicine and tissue engineering are no exception. In this article, we propose a method for finding new double phosphate materials, which is based on machine learning, screening, and applying data from structural databases, and use this methodology combined with chemical knowledge to propose several promising materials for bone tissue engineering. For the selected candidates, we develop a solid-phase synthesis procedure and apply their physical characteristics to confirm the results. In addition, the role of morphology, that is, the porosity of frameworks based on these materials, is discussed from a biomedical point of view, and several synthetic ways to adjust this parameter are proposed and investigated.

Keywords: machine learning, porous structures, graph neural networks, stability prediction, bone implants
DOI: 10.1134/S102745102470023X

INTRODUCTION

Compounds with formula $M1^{II}M2^{IV}(PO_4)_2$ have been intensively studied for several decades for their potential use in the nuclear industry as a matrix for conditioning actinide radioactive waste or as reaction products of spent nuclear fuel with tributyl phosphate during reprocessing.

They have also proven interesting as luminescent materials, the properties of which depend on the relationship between composition and crystal structure [1, 2].

The structure of compounds $M1^{II}M2^{IV}(PO_4)_2$ comes from two different archetypes: cheralite and yavapaiite structures. Cheralite is an anhydrous phosphate mineral with the chemical formula $CaTh(PO_4)_2$; it is isomorphic to hattonite and monazite and was formerly known as brabantite. Yavapaiite has the formula $KFe(SO_4)_2$ with some exceptions, which are also described in the literature [3–5]. The ratio of cation radii $M1$ and $M2$ seems to be the most important parameter. The ratio between the ionic radii of divalent and tetravalent cations in yavapaiite derivatives leads to the ordering of these cations into well-differentiated polyhedra (Fig. 1), while cheralite is the only disordered structure found in compounds of the type $M1^{II}M2^{IV}(PO_4)_2$ and yavapaiite [3, 6–8].

Yavapaiite $KFe^{3+}(SO_4)_2$ crystallizes in the monoclinic space group $C2/m$. The K cation is bonded to ten anions of oxygen O. There is a scatter of K–O bond lengths in the range of 2.88–3.17 Å. The Fe^{3+} cation is bonded to six O atoms to form FeO_6 octahedra, which share vertices with six equivalent SO_4 tetrahedra. Among these bonds, there are two short (1.99 Å) and four longer (2.04 Å) Fe–O bonds. The sulfur atom S is bonded to four O atoms, forming SO_4 tetrahedra, which share vertices with three equivalent FeO_6 octahedra. The angles formed by vertex-sharing octahedra range from 32° to 43°. Also, the scatter of S–O bond lengths is observed in the range of 1.46–1.51 Å. Oxygen occupies three nonequivalent positions. In the first position, the oxygen atom forms a bond with one Fe atom and one S atom, forming an angle of 150°. In the second position, the oxygen atom is bonded in a distorted geometry to three K atoms in equivalent positions and one sulfur atom. In the third position, the oxygen atom is bonded to one K atom, one Fe atom, and one S atom [9].

Cheralite $CaTh(PO_4)_2$ crystallizes in the triclinic space group P-1. The Ca cation is bonded to nine anions of oxygen O. Ca–O bond lengths are in the range of 2.44–2.93 Å. Th is bonded to ten O atoms. Th–O bond lengths vary in the range of 2.41–2.94 Å. The P cation has two equivalent positions. In the first

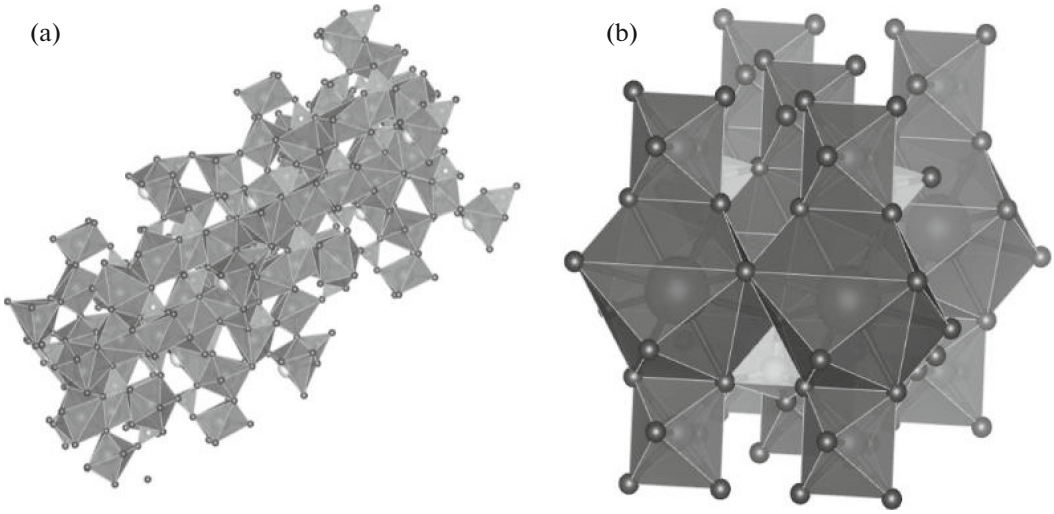

Fig. 1. General view of the crystal structure of $CaTh(PO_4)_2$ (a) and $KFe(SO_4)_2$ (b).

position, the P atom is located in a tetrahedron of O oxygen atoms. The scatter of P–O bond lengths is in the range of 1.54–1.57 Å. In the second position, the P atom is also bonded to four oxygen O atoms in tetrahedral coordination: three bonds are short (1.55 Å) and one bond is longer (1.57 Å). Atoms of oxygen O are located in eight nonequivalent positions. In two positions, the O atom is bonded to two equivalent Ca atoms, one Th atom, and one P atom. In one position, O is bonded to two Th atoms in equivalent positions and one P atom. In four more positions, O forms a bond with one Ca atom, one Th atom, and one phosphorus P atom. In one position, the O atom is bonded to one Ca and two Th atoms in equivalent positions and one P atom. In general, the ferric ion exhibits octahedral distortions characteristic of the anionic type of involvement. The average bond length between ferric iron and oxygen is 2 Å, although in known structures the distance between atoms varies between 1.91–2.24 Å [10].

In the cheralite family, compounds with the formula $M^{II}Ge(PO_4)_2$ are widely unknown, except their cell parameters and the hypothesis about their space groups; refinements are made on the basis of diffraction patterns of the compounds $BaGe(PO_4)_2$ [11], $SrGe(PO_4)_2$ [12], and $CaGe(PO_4)_2$ [1] obtained by solid-phase synthesis.

A series of phosphates with a general formula $A^{II}M^{IV}(PO_4)_2$ (A are alkaline-earth metals; M is Ti, Zr, Ge, Sn, or Mo) [13, 14] can potentially be used as catalysts, ion exchangers, and ionic conductors and for immobilization of high level nuclear waste. In addition, their chemical properties and thermal stability ensure that compounds of this group are potential candidates for the production of luminescent materials [9].

Biphosphate ceramics is used as various anti-osteoporotic drugs for fracture healing [15–17]. Many drugs are now known to include strontium to promote osteoblast-mediated bone formation and inhibit osteoclast-mediated bone resorption and have been widely studied both in vitro and in vivo [16, 18]. Strontium prevents osteoclast-induced bone resorption, as well as osteoclast differentiation [19], and strontium preparations are also used to stimulate the bone-forming function of osteoblasts and preosteoblastic proliferation/differentiation. They increase the expression of collagen type I and osteopontin (OPN), which are important components of the organic bone matrix [20].

$SrGe(PO_4)_2$ has two phases. Low temperature α-$SrGe(PO_4)_2$ (space group $C2/c$, the number of formula units $Z = 4$) is a distorted derivative, and β-$SrGe(PO_4)_2$ ($C2/m$, $Z = 2$) is completely isotypic to yavapaiite [21].

Double phosphates have several advantages as scaffold materials for bone tissue engineering. They have a structure similar to the mineral component of natural bone, making them biocompatible. Additionally, double phosphates have osteoconductive properties, which means that they can support the attachment, proliferation, and differentiation of bone-forming cells. In the context of bone tissue engineering, scaffolds made from double phosphates provide a porous structure that enables cell and nutrient penetration [22]. This allows new tissues to be regenerated, creating a three-dimensional environment that mimics the natural extracellular matrix of bone. Connected pores within the scaffold facilitate cell migration, nutrient exchange, and deposition of extracellular matrix components. In addition, the chemical composition of double phosphates can be tailored to enhance their biological activity and mechanical properties, promoting better integration into the surrounding host tissue [23]. Various techniques can be used to modify the surface properties of double phosphate scaffolds, such as

their coating with bioactive molecules or incorporating growth factors to stimulate bone formation.

Tissue engineering has brought new hope for bone regeneration using a combination of cells, scaffolds, and bioreactors. A synthesized bone scaffold is a three-dimensional matrix that allows and stimulates the attachment and proliferation of osteoinduced cells on its surfaces. When developing bone scaffolds, the following factors must be taken into account: biocompatibility in terms of cell attachment and proliferation, as well as the absence of toxicity and inflammatory reactions; biodegradability for programmed safe replacement of scaffold material by osteoid deposition; mechanical properties that allow one to withstand the load during the recovery period; proper structure in terms of porosity and pore size for cell penetration, nutrient and waste transport, angiogenesis; sterility without loss of biological activity; and controlled delivery of biologically active molecules or drugs [24–29].

Scaffold pore size is a critical parameter that significantly influences scaffold properties and performance in tissue engineering. Pore size selection can influence cellular infiltration, nutrient diffusion, mechanical integrity, and tissue regeneration outcomes [30]. The pore size of the scaffold directly influences cell attachment, migration, and proliferation. Pores that are too small can impede cell penetration and limit the diffusion of nutrients and oxygen, potentially leading to cell death and poor tissue regeneration. Conversely, pores that are too large may not provide sufficient structural support for cell attachment and tissue formation [31]. Therefore, optimal pore size is important to facilitate cell–scaffold interactions and ensures uniform distribution of cells throughout the scaffold. Pore size also influences the mechanical properties of scaffolds. Smaller pore sizes generally increase the mechanical strength and stiffness of the framework, which can be beneficial in load-bearing applications. On the other hand, large pore sizes may reduce mechanical properties but provide increased flexibility and compressibility. It is critical to find a balance between structural integrity and mechanical properties based on the specific requirements of the tissue being regenerated. In addition, pore size influences the vascularization potential of the scaffold. [32]. Smaller pores can restrict blood vessel formation, preventing oxygen and nutrients from reaching regenerating tissue. Larger pores, on the other hand, may promote blood vessel ingrowth and neovascularization, promoting better tissue integration and functionality. Therefore, determining the appropriate pore size is essential to promote vascularization and ensure successful tissue regeneration [33, 34]. Regarding the fabrication of scaffolds, the pore size can be controlled using various methods, such as freeze drying, electrospinning, or 3D printing [34–38]. The choice of fabrication method can allow precise variation of pore size and pore distribution within the scaffold structure.

Traditionally, the discovery and development of these compounds have relied heavily on lengthy experiments and trial and error methods. However, with the advent of machine learning, is a promising new way to speed up the process of discovering new materials has appeared. Machine learning algorithms combined with huge amounts of data can effectively predict the structural characteristics and formation energies of double phosphates and enable targeted synthesis. This combination of computing power and analytical data has enormous potential to revolutionize the development of new materials, such as double phosphates, thereby facilitating breakthroughs in various areas of biomedical applications. This paper discusses the application of machine learning methods to predict double phosphate structures for biomedical applications. We explore the underlying principles, methodologies, and challenges associated with this approach.

Materials and Scaffold Production

We chose solid-phase synthesis as the method for creating samples. The synthesis method is simple to perform, does not require additional reagents, and gives a good product yield [39]. To form ceramics, rapid heating to 600°C and subsequent annealing for 5 h are required. The second stage of synthesis is annealing at a temperature of 1000°C for 5 h for the complete transition of germanium oxide into the desired $SrGeP_2O_8$ ceramics.

The following reagents were used for the synthesis of strontium–germanium phosphate: strontium carbonate ($SrCO_3$, molar mass (M_w) = 147.63 g/mol, 98%, Sigma-Aldrich), germanium (IV) oxide (GeO_2, M_w = 104.61 g/mol, 99%, Sigma-Aldrich), and ammonium dihydrogen orthophosphate ($NH_4H_2PO_4$, M_w = 115.03 g/mol, 98%, Sigma-Aldrich). To create a porous scaffold caffeine ($C_8H_{10}N_4O_2$, M_w = 194.19 g/mol, 99%, Sigma-Aldrich) and crushed luffa (lat. *Lūffa aegyptiaca*) were used as porogens.

The ability of the scaffold to adsorb proteins is one of the main properties affecting the proliferation of the implant. Proliferation is the growth of body tissue by cell multiplication by division. Also, the ability to adsorb affects differentiation of cells, and in the future, their survival. This is why studying the adsorption of scaffold materials is an important task. Albumin was chosen as the protein for the study. Serum albumin is synthesized in the liver, found in human blood, and makes up the majority of all serum proteins (about 55%) contained in blood plasma [40]. To carry out the measurements, in this work, we weighed out 100 mg of caffeine and luffa samples as porogens and then added 10 mL of freshly prepared albumin solution to each beaker. [41]. After this, the time was recorded and 2 mL of the solution was taken using a Mohr pipette

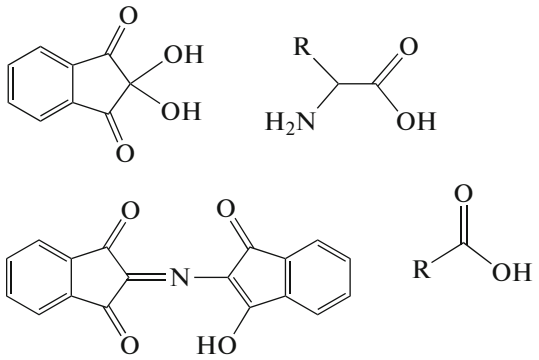

Fig. 2. The schematic reaction of ninhydrin with the amino group of the analyte forms a compound similar to diketohydrazine.

after 30, 60, 90, and 120 min. The selected samples must be placed in a refrigerator.

The concentration of amino acids is usually measured using ninhydrin. Ninhydrin is a strong oxidizing agent. It reacts with all α-amino acids in the pH range from 4 to 8, forming a purple complex [42]. The same reaction is given by primary amines, amino acids, and ammonia, without the release of CO; amino acids proline and hydroxyproline also interact with ninhydrin, but the resulting complex is yellow (Fig. 2). The violet complex (Ruemann purple) can be detected by photocolorimetry at a wavelength of 550 nm; the yellow complex, at a wavelength of 440 nm.

The reaction with ninhydrin is highly sensitive, allowing the determination of amino acid content in chromatograms, as well as columnar fractions with an accuracy of several μg.

Selected samples were reacted with ninhydrin [43]. The optical density of the resulting solution was measured on a KFK-2 photocolorimeter using different wavelengths 540 and 590 nm; based on the data obtained, a calibration dependence of optical density on the amount of albumin in relative units was constructed.

METHODS FOR DETERMINING PHYSICAL CHARACTERISTICS

Powder X-ray Diffraction

X-ray diffraction (XRD) patterns were recorded on a D2 Phaser Advance X-ray diffractometer (Bruker, United States) operating at 40 kV and 30 mA using CuK_α radiation ($\lambda = 0.1542$ nm) . Diffraction patterns were collected at a temperature of 25°C in the angular range from 20° to 70° with a step of 0.05° and a dwell time of 12 s in each position.

Low-Temperature Sorption of N_2

The specific surface area of the materials was analyzed using nitrogen adsorption/desorption isotherms at −196°C measured on an ASAP 2020 accelerated surface area analyzer and a porosimetric analyzer (Micromeritics Instruments Corp., Unite States). Before measurements, the samples were activated at a temperature of 250°C for 10 h in a dynamic vacuum. Nitrogen was used as the adsorbing gas.

X-ray Fluorescence Analysis

Nondestructive elemental analysis of the sample was carried out on a Bruker M4 TORNADO. The selected elements (Ge, Sr, and P) were detected at a voltage of 50 kV and a current of 300 μA.

Machine Learning and Computational Methods

Starting from the initial structures of yavapaiite and cheralite, two groups of candidate materials were created by isoelectronic substitution of atoms in the sublattices of these two materials. The first group was formed by replacing one Ca atom with the following atoms: Mg, Sr, Zn, Ba, Be, Eu, Sm, and Pb in the cheralite structure. The second group was created by simultaneously replacing several atoms in the yavapaiite structure, namely Fe, K, and S atoms with Ge, Sr, and P, respectively. Having different ionic radii, these cations must introduce changes in the structure, especially in the case of multiple substitutions.

To elucidate the stability of the two groups of these compounds, we calculated the energy difference profile for a set of relaxed substituted structures, given that the energy above hull (EAH) for the experimentally observed parent compounds is close to zero. For the sake of a good balance between accuracy and computational cost, a surrogate machine learning model for the interatomic potential was used to calculate the energies and forces. Graph neural network with universal interatomic three-body interaction potential (M3GNet) [44], which is based on the Materials massive project data set, was selected as a modern universal potential for relaxing the structure of a compound after atomic substitution and calculating the energy per atom for each of them (Fig. 3). Experimentally acceptable materials were determined, and their structural features were assessed. Relaxation of the structure was carried out using the conjugate gradient method by simultaneously alternating the cell volume and atomic positions.

RESULTS AND DISCUSSION

The graph neural network with the universal interatomic three-body interaction potential (M3GNet) made it possible to calculate the energy of substituted compounds. As a metric for the stability of a compound, it is common to plot the enthalpy of formation

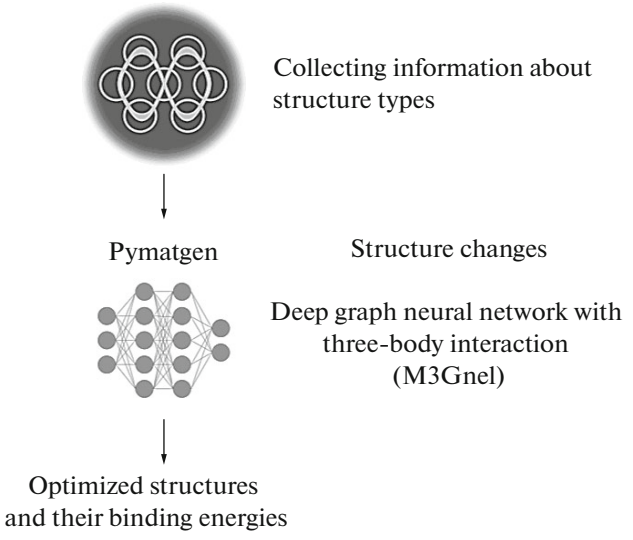

Fig. 3. Schematic illustration of the conveyor for taking away materials using machine learning proposed in the study to find double phosphate structure modifications.

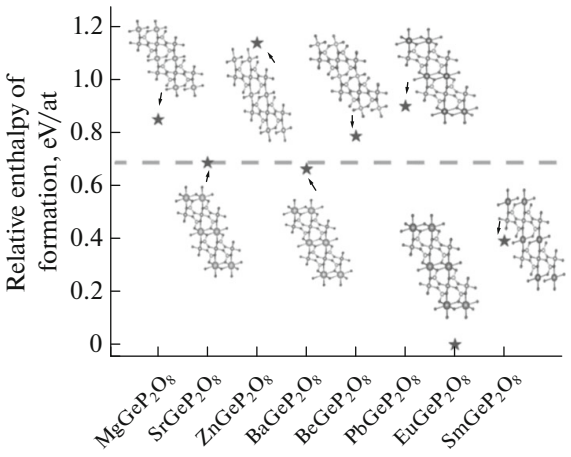

Fig. 4. Distribution of substituted compounds by the enthalpy of formation with a general view of the structure of each of them; the dotted line shows the energy level above the phase stability curve of 0 eV.

as a function of composition, constructing a convex polygon through phases that have less energy than any other phases or their linear combination at a given composition. The phases lying on this convex polygon (convex hull) are thermodynamically stable, and those above it are either metastable or unstable. The magnitude of the difference between the enthalpy of formation of a compound and the point of a convex polygon with the same composition (the energy above the curve of stable phases) quantitatively characterizes the stability of the inorganic compound. Based on these data, we can talk about their stability and preferred substitutions in the composition. The arrangement of compounds by energy is clearly shown (Fig. 4). It can be concluded that the system with Sr as a substituting atom is energy optimal.

All samples were examined by powder X-ray diffraction. The diffraction pattern of the sample used as the base material is shown in Fig. 5a (curve *2*). The data were analyzed using the Jana2006 software [45]. As a result, it was discovered that the material contains $SrGeP_2O_8$ as the main phase (Fig. 5b). According to data (entry in COD 1563127) [4], the structure of this compound belongs to the monoclinic symmetry, space group $C12/m1$ (12). The unit cell parameters were determined, which were a = 7.8611(10) Å, b = 5.0397(7) Å, c = 7.3511(8) Å, and β = 93.833(12)°.

In addition, the sample of the base material contains a small impurity of germanium oxide, which was used as a source of Ge in the synthesis of ceramics. The phase was identified as trigonal, space group $P3_121$ (152), and the cell parameters were $a = b$ = 4.9811(10) Å and c = 5.6273(19) Å.

After adding porogens the samples were examined using X-ray diffraction. It is worth noting that different porogens had different effects on the chemical composition of the original ceramics. Figure 6 shows diffraction patterns: as is seen, in the case of caffeine, the composition of the ceramics changed; a bright peak from germanium oxide appeared at $2\theta = 26°$. The luffa sample did not affect the composition of the ceramics.

Low-temperature nitrogen sorption isotherms were also analyzed to determine the available pore volume and specific surface area of the synthesized materials.

Nitrogen sorption isotherms were measured for the samples. To do this, a weighed portion of the corresponding sample was initially kept at 250°C for 15 h under dynamic vacuum conditions to remove guest molecules from the pores. Next, nitrogen adsorption-desorption isotherms were measured at a temperature of −196°C.

Both isotherms obtained are classified as type II, according to the IUPAC classification. [46]. At low pressures, the sorption isotherm behaves similar to the type I isotherm; that is, monomolecular adsorption occurs on active areas of the sorbent surface. Additional layers of adsorbate molecules are formed gradually, and the isotherm reaches a plateau. This means that the surface of the sorbent is saturated with adsorbate molecules and additional layers no longer lead to a significant increase in the adsorption volume. Type II isotherms are characteristic of materials with mesopores (pores with sizes from 2 to 50 nm). In addition, type II reversible isotherm without a pronounced step in the low-pressure region is a typical form of the isotherm of nonporous or macroporous (up to 1 nm in size) materials.

The Langmuir model was used to calculate the specific surface area. Although, according to the measured isotherms, the resulting materials may contain

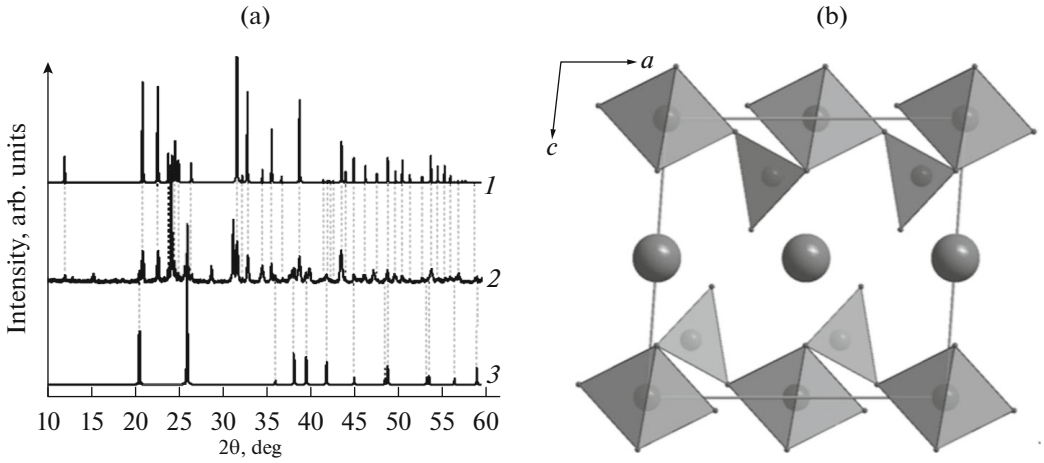

Fig. 5. (a) Diffraction patterns of the synthesized $SrGeP_2O_8$ (*2*); for comparison the calculated profiles are given for germanium oxide (*3*) and $SrGeP_2O_8$ (*1*). (b) Unit cell model of the $SrGeP_2O_8$ structure: large spheres represent Sr, tetrahedra represent PO_4, and the gray octahedra represent GeO_6.

meso- and macropores containing several layers of nitrogen molecules, saturation plateau positions indicate low porosity of the ceramics. Thus, the formation of multilayers of sorbed N_2 molecules can be neglected. This makes the Langmuir model more suitable for calculating the specific surface area of the materials under consideration (Fig. 7).

It was found that the sample containing caffeine as a porogen showed higher porosity than the sample with luffa.

For a more complete picture, X-ray phase analysis of the obtained materials was carried out. The data on the percentage content of elements are presented in Table 2. From the elemental analysis data it is clear that the materials are identical in chemical composition and the porogen does not have a significant effect on the elemental composition of the ceramics.

The study of protein adsorption on the surface of the material allows us to draw conclusions about the possibilities of using the material. Since the research is aimed at developing materials for implants, protein adsorption should be considered an important characteristic. This parameter has a significant impact on the proliferation of patient tissue on the surface of the implant. In addition, the ability to adsorb protein on the surface affects the survival rate of the implant, whether it can provide the ability to attach cells to the surface. A graph of protein adsorption versus time is presented in Fig. 8.

As can be seen from the graph, the sample with caffeine adsorbs protein in a fairly large amount; depending on time the concentration of adsorbed protein increases. In the case of luffa, the situation is completely different: the material does not adsorb protein

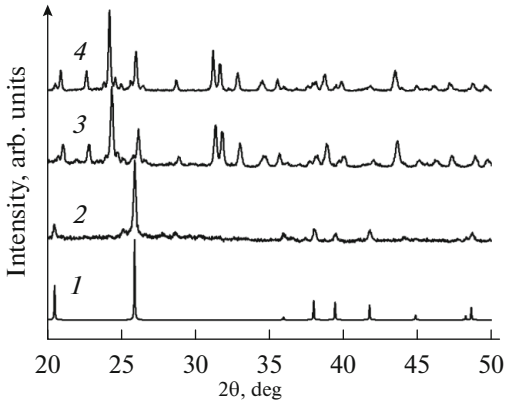

Fig. 6. X-ray diffraction patterns of samples: initial ceramics (*4*), samples with porogens luffa (*3*) and caffeine (*2*), and germanium oxide (*1*).

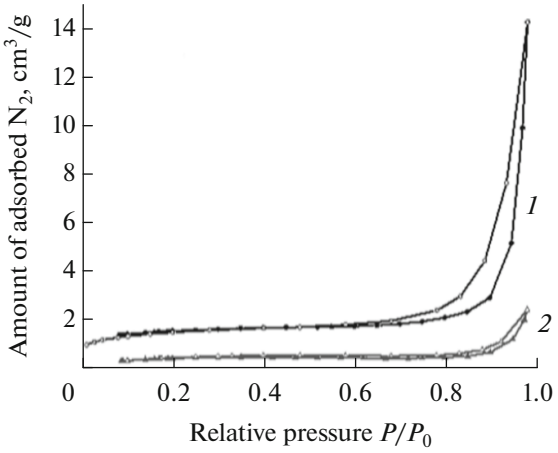

Fig. 7. N_2 adsorption–desorption isotherms for samples with caffeine (*1*) and luffa (*2*).

Table 1. Data calculated from the adsorption isotherms of the synthesized samples. Pore volume is given for relative pressure $P/P_0 = 0.975$. Specific surface area was calculated according to the Langmuir model

Porogen	Pore volume, cm^3/g	Specific surface area, m^2/g	Langmuir constant b, $(mmHg)^{-1}$	Adsorption monolayer capacity Qm, cm^3/g	Correlation coefficient
Caffeine	0.0153	7.6	0.060	1.75	0.99976
Luffa	0.0031	2.62	0.019	0.60	0.99934

Table 2. Elemental analysis results for materials with porogens

Porogen	Content, %		
	Sr	Ge	P
Caffeine	30.04	28.76	41.2
Luffa	31.12	29.86	39.2

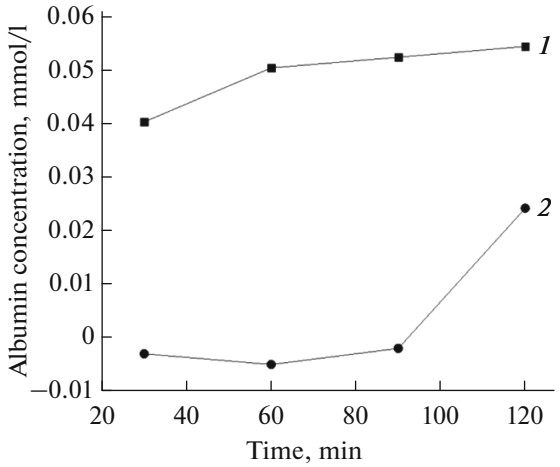

Fig. 8. Graph of albumin adsorption by samples with caffeine (*1*) and luffa (*2*) as a function of time.

during the first 1.5 h, after which a sharp jump in protein adsorption occurs.

CONCLUSIONS

Using the graph neural network M3GNet the most stable substituted structures of the minerals yavapaiite and charolite were found. The most stable structure turned out to be one, in which K was replaced by Sr and Fe was replaced by Ge. Based on theoretical stability studies, this system was chosen for the solid-phase synthesis of ceramics for bioapplications. In addition, Sr in bioceramics has a positive effect on the recovery process. Preparations containing strontium are actively used to treat bone defects. $SrGeP_2O_8$ was obtained by solid-phase synthesis. Based on it, materials with the addition of porogens were also synthesized. The structure of the compounds was studied using powder X-ray diffraction. Diffraction of the samples with porogens made it possible to find out that, depending on the porogen, the composition of the original ceramics can change. The addition of caffeine as a porogen made it possible to obtain a material with a specific surface area of 7.6 m^2/g, which is 3 times the surface area of the material with luffa. The sample with caffeine has good properties for protein adsorption on the surface. This was demonstrated by the experiment on protein adsorption; the material accumulates protein gradually, increasing accumulation over time. Based on these data, it can be concluded that the material is promising for practical use as ceramics for medical implants.

FUNDING

The work was supported by the Russian Science Foundation (project no. 23-21-00331).

CONFLICT OF INTEREST

The authors of this work declare that they have no conflicts of interest.

REFERENCES

1. D. Bregiroux, K. Popa, and G. Wallez, J. Solid State Chem. **230**, 26 (2015). https://www.doi.org/10.1016/j.jssc.2015.06.010
2. F. Tudorache, K. Popa, L. Mitoseriu, N. Lupu, D. Bregiroux, and G. Wallez, J. Alloys Compd. **509**, 9127 (2011).
3. E. D. F. Kerdaniel, PhD Thesis (Universite Paris XI UFR Scientifique D'Orsay, 2007).
4. K. Popa, G. Wallez, D. Bregiroux, and P. Loiseau, J. Solid State Chem. **184** (10), 2629 (2011). https://www.doi.org/10.1016/j.jssc.2011.07.037
5. A. Tabuteau, M. Pages, J. Livet, and C. Musikas, J. Mater. Sci. Lett. **7** (12), 1315 (1988). https://www.doi.org/10.1007/BF00719969
6. K. Popa, G. Wallez, P. E. Raison, D. Bregiroux, Ch. Apostolidis, Lindqvist-Reis P., and R. J. M. Konings, Inorg. Chem. **49** (15), 6904 (2010). https://www.doi.org/10.1021/ic100376u
7. G. Wallez, D. Bregiroux, K. Popa, P. E. Raison, Ch. Apostolidis, P. Lindqvist-Reis, R. J. M. Konings, and A. F. Popa, Eur. J. Inorg. Chem. **2011** (1), 110 (2010). https://www.doi.org/10.1002/ejic.201000777
8. Z.-J. Zhang, H.-H. Chen, X.-X. Yang, J.-T. Zhao, G.-B. Zhang, and Ch.-Sh. Shi, J. Phys. D: Appl. Phys. **41**, 105503 (2008). https://www.doi.org/10.1088/0022-3727/41/10/105503

9. A. M. Ganose and A. Jain, MRS Commun. **9** (3), 874 (2019). https://www.doi.org/10.1557/mrc.2019.94
10. W. Pies and A. Weiss, *References for III/7*, Vol. 7G: *Landolt-Börnstein – Group III Condensed Matter*, Ed. by K.-H. Hellwege and A. M. Hellwege, (Springer, Berlin, 1971–1972). https://www.doi.org/10.1007/10201585_20
11. E. Morin, G. Wallez, S. Jaulmes, J. C. Couturier, and M. Quarton, J. Solid State Chem. **137** (2), 283 (1998). https://www.doi.org/10.1006/jssc.1997.7735
12. K. Popa, R. J. M. Konings, D. Bouexiere, A. F. Popa, and T. Geisler, Adv. Sci. Technol. **45** 2012 (2006). https://www.doi.org/10.4028/www.scientific.net/AST.45.2012
13. Y. Huang, Y. Cao, Ch. Jiang, L. Shi, Y. Tao, and H. J. Seo, Jpn. J. Appl. Phys. **47**, 6364 (2008). https://www.doi.org/10.1143/jjap.47.6364
14. K. Popa, R. J. M. Konings, O. Benes, T. Geisler, and A. F. Popa, Thermochim. Acta **451** (1–2), 1 (2006). https://www.doi.org/10.1016/j.tca.2006.08.011
15. S. Larsson and N. L. Fazzalari, Arch. Orthop. Trauma Surg. **134** (2), 191 (2014). https://www.doi.org/10.1007/s00402-012-1558-8
16. P. J. Marie, Bone **40** (5), 5 (2007). https://www.doi.org/10.1016/j.bone.2007.02.003
17. W. Querido, A. L. Rossi, and M. Farina, Micron **80**, 122 (2016). https://www.doi.org/10.1016/j.micron.2015.10.006
18. A. Doublier, D. Farlay, M. T. Khebbab, X. Jaurand, P. J. Meunier, and G. Boivin, Europ. J. Endocrinol. **165** (3), 469 (2011). https://www.doi.org/10.1530/EJE-11-0415
19. R. Baron and Y. Tsouderos, Eur. J. Pharmacol. **450** (1), 11 (2002). https://www.doi.org/10.1016/s0014-2999(02)02040-x
20. M. S. Rybchyn, M. Slater, A. D. Conigrave, and R. S. Mason, J. Bio. Chem. **286** (27), 23771 (2011). https://www.doi.org/10.1074/jbc.M111.251116
21. H. Bellefqih, R. Fakhreddine, R. Tigha, and A. Aatiq, Mediterr. J. Chem. **10** (8), 2020. https://www.doi.org/10.13171/mjc10802108201448hb
22. J. H. Shepherd and S. M. Best, JOM **63** (4), 83 (2011). https://www.doi.org/10.1007/s11837-011-0063-9
23. L. L. Hench and J. M. Polak, Science **295** (5557), 1014 (2002). https://www.doi.org/10.1126/science.1067404
24. S. Amin, S. J. Achenbach, E. J. Atkinson, S. Khosla, and L. J. Melton, J. Bone Mineral Res. **29** (3), 581 (2014). https://www.doi.org/10.1002/jbmr.2072
25. B. N. Brown, J. E. Valentin, A. M. Stewart-Akers, G. P. McCabe, and S. F. Badylak, Biomaterials **30** (8), 1482 (2009). https://www.doi.org/10.1016/j.biomaterials.2008.11.040
26. D. W. Hutmacher, Biomaterials **21** (24), 2529 (2000). https://www.doi.org/10.1016/s0142-9612(00)00121-6
27. T. Kokubo, H. M. Kim, and M. Kawashita, Biomaterials **24** (13), 2161 (2003). https://www.doi.org/10.1016/s0142-9612(03)00044-9
28. J. R. Porter, T. T. Ruckh, and K. C. Popat, Biotechnol. Prog. **25** (6), 1539 (2009). https://www.doi.org/10.1002/btpr.246
29. J. Y. Rho, L. Kuhn-Spearing, and P. Zioupos, Med. Eng. Phys. **20** (2), 91 (1998). https://www.doi.org/10.1016/s1350-4533(98)00007-1
30. C. Gao, Y. Deng, P. Feng, Zh. Mao, P. Li, B. Yang, J. Deng, Y. Cao, C. Shuai, and Sh. Peng, Int. J. Mol. Sci. **15** (3), 4714 (2014). https://www.doi.org/10.3390/ijms15034714
31. F.-H. Liu, J. Sol-Gel Sci. Technol. **64** (3), 704 (2012). https://www.doi.org/10.1007/s10971-012-2905-5
32. S. Preethi Soundarya, A. Haritha Menon, S. Viji Chandran, et al., Int. J. Biol. Macromol. **119**, 1228 (2018). https://www.doi.org/10.1016/j.ijbiomac.2018.08.056
33. J. M. Seok, T. Rajangam, J. E. Jeong, and N. Selvamurugan, J. Mater. Chem. B **8**, 951 (2020). https://www.doi.org/10.1039/c9tb02360g
34. A. A. Zadpoor, Biomater. Sci. **3** (2), 231 (2015). https://www.doi.org/10.1039/c4bm00291a
35. X. Chen, H. Fan, X. Deng, L. Wu, T. Yi, L. Gu, Ch. Zhou, Y. Fan, and X. Zhang, Nanomaterials **8** (11), 2018. https://www.doi.org/10.3390/nano8110960
36. Y. Javadzadeh and S. Hamedeyazdan, *Trends in Helicobacter pylori Infection*, Ed. by B. M. Roesler (InTech, 2014). https://www.doi.org/10.5772/57353
37. M. Mabrouk, T. G. El-Bassyouni, H. Beherei, and S. H. Kenawy, *Advanced 3D-Printed Systems and Nanosystems for Drug Delivery and Tissue Engineering* (Elsevier, 2020), p. 83.
38. G. Tripathi and B. Basu, Ceram. Int. **38** (1), 341 (2012). https://www.doi.org/10.1016/j.ceramint.2011.07.012
39. S. Pramanik, A. K. Agarwal, K. N. Rai, and A. Garg, Ceram. Int. **33** (3), 419 (2007). https://www.doi.org/10.1016/j.ceramint.2005.10.025
40. G. J. Merli and H. H. Weitz, *Medical Management of the Surgical Patient* (Elsevier, 2008).
41. Y. I. Hao, Vox Sanguinis **36** (5), 313 (2009). https://www.doi.org/10.1111/j.1423-0410.1979.tb04441.x
42. S. Jeong, Y. Jeon, J. Mun, S. M. Jeong, H. Liang, K. Chung, P.-I. Yi, Chemosensors **11** (1), 49 (2023). https://www.doi.org/10.3390/chemosensors11010049
43. F. D. Lasky, Z. M. C. Li, D. D. Shaver, J. Savory, M. G. Savory, D. G. Willey, B. J. Mikolak, and Ch. L. Lantry, Clin. Biochem. **18** (5), 290 (1985). https://doi.org/10.1016/S0009-9120(85)80034-5
44. C. Chen and S. P. Ong, Nat. Comput. Sci. **2** (11), 718 (2022). https://www.doi.org/10.1038/s43588-022-00349-3
45. V. Petříček, M. Dušek, and L. Palatinus, Z. Kristallogr. **229** (5), 345 (2014). https://www.doi.org/10.1515/zkri-2014-1737
46. K. S. W. Sing, Pure Appl. Chem. **57** (4), 603 (1985). https://www.doi.org/10.1351/pac198557040603